Concentration and velocity statistics of inertial particles in upward and downward pipe flow

J. L. G. Oliveira[1],‡, C. W. M. van der Geld[2],† and J. G. M. Kuerten[1,3]

[1]Department of Mechanical Engineering, Eindhoven University of Technology, P.O. Box 513, 5600 MB Eindhoven, The Netherlands

[2]Department of Chemical Engineering and Chemistry, Eindhoven University of Technology, The Netherlands

[3]Faculty EEMCS, University of Twente, The Netherlands

Three-dimensional particle tracking velocimetry is applied to particle-laden turbulent pipe flows at a Reynolds number of 10 300, based on the bulk velocity and the pipe diameter, for developed fluid flow and not fully developed flow of inertial particles, which favours assessment of the radial migration of the inertial particles. Inertial particles with Stokes number ranging from 0.35 to 1.11, based on the particle relaxation time and the radial-dependent Kolmogorov time scale, and a ratio of the root-mean-square fluid velocity to the terminal velocity of order 1 have been used. Core peaking of the concentration of inertial particles in up-flow and wall peaking in down-flow have been found. The difference in mean particle and Eulerian mean liquid velocity is found to decrease to approximately zero near the wall in both flow directions. Although the carrier fluid has all of the characteristics of the corresponding turbulent single-phase flow, the Reynolds stress of the inertial particles is different near the wall in up-flow. These findings are explained from the preferential location of the inertial particles with the aid of direct numerical simulations with the point-particle approach.

1. Introduction

Turbulent dispersed two-phase flows are abundant in both industry and nature. Dispersion of pollutants in an urban environment, sediment transport and the fluidized catalytic cracking of carbohydrates are, for example, of major importance. The ability to predict the migration of a dispersed phase with a different velocity from the carrier phase, with either numerical or analytical models, is required in a wide range of disciplines. A thorough understanding of the behaviour of this type of dispersed two-phase flow in practice is essential for model development, and facilitates scale-up

† Email address for correspondence: C.W.M.v.d.Geld@tue.nl

‡ Present address: Mobility Department, Federal University of Santa Catarina, Joinville/SC, 89218-000, Brazil.

of process equipment and improvement of mixing efficiencies. It is clear that a consistent set of experimental data under well-known conditions is needed to validate models. The present study aims to increase our understanding and provide such a set of data. Before describing the main features of the approach followed, previous experimental work and relevant theoretical studies are first reviewed.

All turbulent flows are inhomogeneous in practice. Although experiments of any kind are useful to reveal the underlying physics of dispersed two-phase flows, experiments on inhomogeneous flows are therefore particularly significant. The most familiar example of such flows is turbulent flow in pipes. Although particle-laden flow in pipes has numerous engineering applications, only restricted classes of turbulent dispersed flows in pipes have been investigated, and to a limited extent. These will be reviewed first.

A significant number of experimental studies have been performed with small solid particles in wall-bounded flows, pipes or channels; small here means with a size of the order of the Kolmogorov length scale or less. Most of the particles have possessed a significant relaxation time scale due to high mass density ratios, as for solid particles in gas flows. The characteristics of both the carrier fluid phase and small solid particles have been measured in turbulent wall-bounded flows by Tsuji & Morikawa (1982), Tsuji, Morikawa & Shiomi (1984), Kulick, Fessler & Eaton (1994), Paris & Eaton (2001), Kussin & Sommerfeld (2002), Caraman, Borée & Simonin (2003), Benson, Tanaka & Eaton (2005), Borée & Caraman (2005) and Yang & Shy (2005). In these studies, attempts were made to explain particle migration, preferential concentrations and turbulence modulation. So-called instantaneous realizations of the fluid velocity field, instantaneous 3D snapshots of the flow field, were combined in the analysis with considerations of particle inertia. Some of these analyses also considered the effects of wake interaction, wall roughness and inter-particle and particle–wall collisions. The latter are of course only significant with high particle loadings. To avoid the need to investigate many different phenomena, it is wise to pay attention to flows with a low concentration of particles. Flows in which the collision frequency, breakage efficiency, agglomeration, reaction rate, deposition or entrainment of particles is essential will therefore not be addressed in the present study.

As opposed to the above small and heavy particles, near-neutrally buoyant particles with significant dimension have less often been investigated. In this case, the particle diameter to Kolmogorov length-scale ratio is high, which induces a high relaxation time once again. An example is polystyrene particles in water flows. The dynamics of such particles in turbulent transport has been the subject of experimental research in more recent studies by Brown, Warhaft & Voth (2009) and Volk *et al.* (2011). These studies concerned counter-rotating disk flow with neutrally buoyant particles. The particle inertia is quite high due to the added mass and the particle size. At the expense of having large-sized particles, the relative velocity is kept limited by selecting a particle mass density, ρ_p, close to that of water. Calzavarini *et al.* (2009) developed a numerical model to predict features of neutrally buoyant particles in a stationary homogeneous isotropic flow. They obtained good agreement with the experimental data of Voth *et al.* (2002) and Qureshi *et al.* (2007) regarding particle acceleration variances. To the best of our knowledge, there are only few experiments with inertial particles with a notable velocity relative to the fluid in turbulent inhomogeneous shear flows. Sato & Hishida (1996) and Suzuki, Ikenoya & Kasagi (2000) studied flows of glass, cellulose and ceramic particles in water with a particle to fluid mass density ratio of approximately 1.5–4. These were channel and not pipe flows. Particle inertia and volume load effects were found to be manifested through changes of several terms in the turbulence kinetic energy equation.

Let U_{TV} be the magnitude of the terminal velocity of the dispersed phase and let u_{rms} be the root-mean-square velocity of the carrier phase. A rather complex motion of bubbles in turbulent flows has been found (Sene, Hunt & Thomas 1994; Spelt & Biesheuvel 1997) to result from the interaction of the turbulent flow and particle inertia when $u_{rms}/U_{TV} = O(1)$. Entrapment of bubbles or particles in vortical flow structures and transport of dispersed phase towards the flowing edges of eddies were found to modify the mean rise velocity of bubbles in homogeneous turbulence. More recently, Aliseda & Lasheras (2011) investigated preferential concentration of bubbles in homogeneous turbulence. The reduction of the rising velocity of bubbles was shown to be related to higher levels of turbulence. All of the above studies with a lighter dispersed phase (bubbles) were performed in isotropic turbulence or in plane shear flows. These studies raise expectations concerning flows with a heavier dispersed phase and terminal velocities of the same magnitude as turbulent fluctuation velocities. If not only the turbulence level but also the lift force, by definition perpendicular to the relative velocity of the particle, were important, differences between bubbles and particles would be expected since the relative velocity has a different sign. In addition, up-flow and down-flow would yield opposite results. In the present study, solid particles slightly heavier than the carrier phase are investigated in both up-flow and down-flow in a pipe; the shape of the particles is constant, their size is well known and the bulk Reynolds number of the fluid is taken to be constant. In particular, the preferential concentration, mean relative velocity and Reynolds stresses of both phases are investigated.

Aliseda & Lasheras (2011) presented a cartoon to explain the mean relative velocity reduction of bubbles in a simplified way. They limited the interaction of bubbles and carrier fluid to two-dimensional (2D) large eddies and considered the residence time of bubbles in these eddies. Adaptation of the approach of Aliseda & Lasheras to vertical particle-laden pipe flow is straightforward and shows that the interaction of inertial particles (with $\rho_p/\rho_f \approx 1.05$, where ρ_f is the mass density of the fluid) with relatively large turbulent flow structures leads to an increased residence time in regions where the eddy velocity is upward and reduces the relative velocity, on average. However, it is far more accurate to resolve all length and velocity scales in direct numerical simulation (DNS) and compute trajectories of inertial particles with the aid of a Lagrangian model of particle motion. This is the approach followed in the present study to investigate the mechanisms that reduce the Eulerian mean relative velocity of particles with respect to the fluid near the pipe wall. This approach increases our understanding and facilitates interpretation of experimental findings. Because of the Lagrangian numerical model used in this study, some relevant models in the literature are briefly examined below.

Attempts to model particle-laden flows have been made numerically in the last two decades. When particles with a size exceeding the Kolmogorov length scale reside in a carrier flow, the only way to fully describe the momentum exchange of the two phases is to resolve the stresses at the particle surfaces. This approach obviously requires large memory and a high processing speed. Commonly, simple geometries with a limited numbers of particles have been studied; see Tryggvason *et al.* (2001) and Dijkhuizen, Van Sint Annaland & Kuipers (2010). More recently, Picano, Breugem & Brandt (2015) performed DNS in a turbulent channel flow with dense suspensions. Other DNS simulations have utilized significant simplifications, e.g. neglect of the effect of the finite size of the particle on the flow and the assumption of a point-force approach for the particle equation of motion; see Poelma (2004). To predict trajectories in a point-particle approach, the total force on a particle must be determined, which makes computation of particle trajectories in DNS possible. In the

point-particle approach, a lift force is usually taken into account. After the famous work of Saffman (1965) for laminar flows, Auton, Hunt & Prud'homme (1988) extended the form of the lift force to high-Reynolds-number flows. As Legendre & Magnaudet (1998) have shown, the form of the lift force given by Auton *et al.* (1988) may be used for all particle Reynolds numbers provided that the lift force coefficient is made dependent on this Reynolds number. The analysis of the present study will focus on explanations of the trends observed experimentally and will use DNS and the point-particle approach. To be clear about this limitation, the DNS of the present study will be named point-particle DNS (PP-DNS). The use of one-way coupling in this numerical model will be validated with experimental results.

Preferential concentration of particles will be seen to play an important role. Turbophoresis, on the other hand, is a very slow process and requires a large development length. Turbophoresis is a much weaker phenomenon than radial particle transport by the lift force component which mainly depends on the derivative of the mean axial velocity with respect to the radial coordinate. Moreover, turbophoresis would yield identical concentrations in up-flow and down-flow, whereas different concentration profiles will be shown to result from this study.

Three-dimensional particle tracking velocimetry, 3D-PTV, is applied to measure fluid–particle interaction and preferential concentration for pipe flows with near-neutrally buoyant particles (with $\rho_p/\rho_f \approx 1.05$) with low and homogeneous inlet concentration. The inertial nature of the particles is mainly due to their size, which ranges from 1.3 to 3.5 times the Kolmogorov length scale. The choice of PTV is justified for the following reasons: the presence of two differently sized particles in the same experiment, the sparseness of the particle fields, the acquisition of simultaneous particle information at different locations across a fairly large measurement volume and the inhomogeneous nature of pipe flow which requires particle statistics collected at discrete radial positions. All flows have a Reynolds number (Re_b) of 10 300, based on the bulk velocity and the pipe diameter.

The structure of the paper is as follows. In § 2, the experimental set-up is presented, including the specifications of the flow tracers and inertial particles, a description of the experimental conditions is given and the numerical method is described. In § 3, results are presented and analysed with the aid of PP-DNS results. The PP-DNS enables the calculation of statistics of fluid velocities evaluated at the particle positions, which are relevant for analysis of the forces acting on a particle and which are virtually impossible to obtain experimentally. The focal points are inertial particle concentration profiles, Eulerian mean velocity differences and the Reynolds stresses of inertial particles. Finally, the main conclusions are stated in § 4.

2. Experimental set-up

2.1. *Test rig*

Turbulent particle-laden pipe flows were created in a water loop driven by a centrifugal pump; see figure 1. The in-line 3 kW centrifugal pump of type DPV18-30, manufactured by 'Duijvelaar pompen', allowed Reynolds numbers, based on the bulk velocity, U_b, and pipe diameter, D, in the range 10^3–10^5.

A set of valves was arranged in such a way that downward and upward vertical flows were possible. A frequency controller permitted fine-tuning of the Reynolds number by adjusting the mass flow rate. The mass flow rate was measured by means of a Micro Motion Elite CMF300 mass flow (Coriolis meter) and mass density meter, whose inaccuracy was less than 0.5 % of the registered flow rate. A water reservoir

Water tank II — 0.15 m³

Removable flow straightener II: bundle type

Removable pipe section for calibration purposes

Test section

~20D

Removable flow straightener I: bundle type

~45D

Water tank I — 2 m³

Coriolis flow meter

Return pipe

CV2
CV3

CV1

~50D

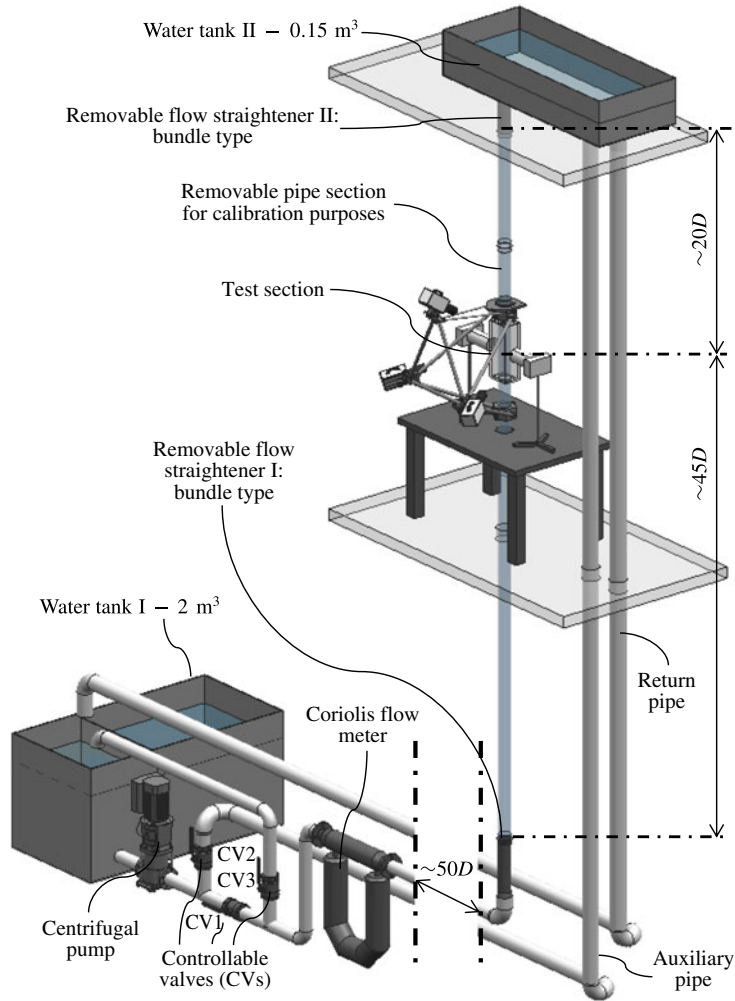Centrifugal pump

Controllable valves (CVs)

Auxiliary pipe

FIGURE 1. (Colour online) Schematic of the experimental 3D-PTV set-up for downward or upward particle-laden pipe flow.

(tank I) was located at the bottom of the set-up and contained approximately 2 m³ of water. This volume facilitated water temperature stabilization and Reynolds number control. The temperature during a test-run was essentially constant, varying by 0.1 °C at most. Submerged pumps were placed in the reservoir tanks at the bottom and the top (tank II, 0.15 m³) of the set-up in order to promote homogeneous dispersion of the added tracers and inertial particles.

The measurement section consisted of a glass pipe to ensure optical accessibility. A water-filled rectangular glass box around the pipe minimized optical distortion. The pipe inner diameter, $D = 2R$, was 100 mm and its wall thickness was 10 mm. Flow straighteners, tube bundle conditioners of ISO 5167-1:1991, see Miller (1996), were employed to avoid secondary flows due to bends. As a result, nearly uniform fluid velocity profiles were obtained just after the flow straighteners. In up-flow, 3D-PTV

measurements were performed at $45D$ downstream of the entrance section; in down-flows, at $20D$.

Three 'HighSpeedStar' cameras with 12-bit greyscale CMOS sensors and a resolution of 1024×1024 pixels were utilized to capture instantaneous 3D particle positions in a measurement volume of $10 \times 10 \times 10$ cm^3. The cameras could record at 1000 Hz at full resolution, but were operated at 50 Hz to maximize the flow measurement time. Recordings were performed until the internal memory of the cameras became full after approximately 2 min. The maximum physically relevant frequencies were approximately 12 Hz for $Re_b = 10\,300$, making a 50 Hz sampling rate sufficient according to the Nyquist theorem. The lighting system comprised two stroboscopic light sources with an output of 5 J per pulse; see figure 1. The strobes were custom-built to maximize the light output at a maximum of 60 Hz with a light pulse duration of approximately 40 µs.

2.2. *Settings and accuracy of 3D-PTV*

While a minimum depth of field of the camera and lenses must be guaranteed to obtain sharp images of moving particles in the whole volume of the measurement section, a certain field of view is needed to obtain trajectories long enough to measure all relevant flow scales. A focal length of 105 mm, an exposure time of 20 µs and a distance from the lens to the object of roughly 800 mm were selected. The sensor resolution was 1 pixel$^2 = 17$ µm $\times$ 17 µm, which corresponds to an actual area of 100 µm $\times$ 100 µm.

To determine the so-called calibration functions that correlate the pixel information from the three cameras to 3D world coordinates, an *in situ* calibration unit was designed. A calibration plate manufactured from a 2.5 mm thick glass plate with a single-sided coating of chromium, 150 nm thick, was given fixed positions at 26 locations in the pipe, interspaced by 2 mm, with a position error of less than 1 µm. Only motion perpendicular to the calibration plate was possible. A 2D array of circular gaps with a diameter of 0.3 mm covered the plate; the centres were 5 mm apart both horizontally and vertically. Third-order polynomials were found to be sufficient to connect the recorded pixel coordinates to actual positions; fitting errors were less than 0.05 pixel.

A commercial 3D-PVT imaging code from La Vision GmbH, named Davis, was used to obtain the trajectories of the tracers and inertial particles. Algorithmic details of the Davis PTV tracking code can be found in Dracos (1996) and Maas (1996). Built-in imaging filters were used to improve the contrast between the tracers and the background. The 2D determination of the centre of a particle in the camera plane was made by a Gaussian fit. The so-called triangulation error is a measure of uncertainty of the 3D particle position. In the present measurements, the maximum triangulation error was 0.2 pixel, roughly 20 µm.

The particle tracking algorithm yields matrices that contain time reference and spatial positions of particle trajectories from the flow measurement images. Before the statistical analysis of turbulent pipe flow is carried out, the spatial positions are converted from Cartesian to cylindrical coordinates with radial coordinate r and azimuthal coordinate θ. In the proximity of the pipe centreline, $r/R = 0$, the discontinuity of radial and tangential velocities for cylindrical coordinates can cause wrong differentiation of displacements in time. Let dt be the timestep between consecutive measurements and let suffix j number the time of measurement, t_j. If a particle crosses $r = 0$, the radial velocity, u_r, may appear to be zero, and the tangential velocity, $u_\theta \approx \pi r/dt$; see (2.1) and (2.2). This problem is avoided by employing a Cartesian frame of reference around the tube axis,
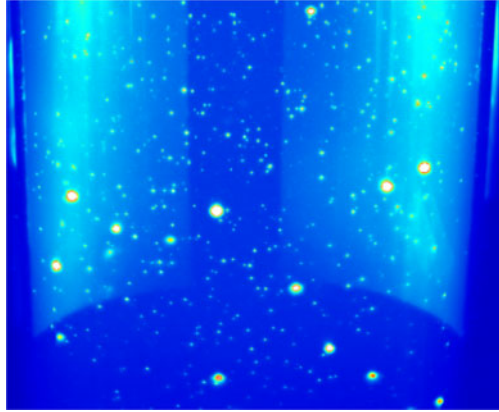
FIGURE 2. (Colour online) One out of three simultaneous recordings of particle-laden flow in the test section; frontal top camera. The inertial particles are the larger circles.

$$u_r(t_j) = [r(t_{j+1}) - r(t_j)]/dt, \qquad (2.1)$$
$$u_\theta(t_j) = [\theta(t_{j+1}) - \theta(t_j)]r(t_j)/dt. \qquad (2.2)$$

After the coordinate transformation, the differentiation in time of the validated trajectories generates the velocity vectors. In a similar way, accelerations were derived from smoothed velocity histories; see Oliveira, van der Geld & Kuerten (2015). Velocities derived by straightforward interpolations of consecutive 3D positions of a particle trajectory have been proved to be reliable to obtain pipe flow statistics. The uncertainty in the magnitude of the velocity vector obtained from two consecutive positions is for both tracers and particles approximately 0.06 mm s^{-1}. Unrealistic trajectories are avoided by two filters: a length filter and an outlier check of five times the standard deviation of the velocity components. The length filter consists of elimination of particle trajectories comprising less than 10 positions. Mean and maximum particle trajectories consist of 30 and 81 positions respectively. More information about the particle tracking algorithm used to obtain the trajectories of the tracers and the inertial particles and the trajectory analysis method for individual particle trajectories is given by Oliveira (2012) and Oliveira, van der Geld & Kuerten (2013).

The number of tracer trajectories measured in the range $r/R = 0.6$–1 decreases with increasing r. The difficulties in measuring tracer trajectories in this region were mainly due to light reflections stemming from the difference between the refractive indices of water, $n \approx 1.33$, and glass, $n \approx 1.51$, and the curvature of the glass pipe. Light reflections deteriorate the contrast between tracers and background. However, the fluid flow could also be measured for $r/R > 0.6$ despite the lower number of usable tracers there. The measured concentration of tracers is roughly linear from $r/R = 0$ to 0.6 and decreases towards the wall for $r/R > 0.6$ for all flow cases. In Oliveira *et al.* (2013), Eulerian statistics of a single-phase turbulent pipe flow acquired by 3D-PTV were found to be trustworthy in the near-wall zone if the number of velocity vectors per radial bin exceeded 1000. The same criterion is also applied in the present work.

In the detection of inertial particle trajectories, the above contrast problem between particles and background did not occur. The larger imaging projection area of inertial particles on the camera sensor, exceeding the projection of tracers by a factor

of 16, avoided problems in the identification of particles; see figure 2. While the projection of a tracer image covers an area of nearly 2×2 pixels, the projection of an inertial particle covers 8×8 pixels. Roughly, every 3D inertial particle position identified in the tracking algorithm corresponds to a real particle. On average, approximately 3×10^5 inertial particle positions were identified in each particle-laden case. Three-dimensional particle positions were identified with a camera frame rate of 50 Hz in average time intervals of 50 min. In this period of time, a water volume corresponding to ≈ 2.3 m^3 crosses the test section. In this way, accurate measurements of concentration profiles of inertial particles were obtained.

The derivative of particle trajectories with respect to time generates on average 2×10^6 velocity vectors for tracers and 3×10^5 for inertial particles in each particle-laden case. The velocity vectors are ensemble-averaged in radial bands with a width of $\Delta r = 1$ mm, except for the first bin, which extends from $r = 0$ to $r = 0.5$ mm; see Oliveira *et al.* (2013). A cylindrical coordinate system (r, θ, z) with origin at the pipe centreline and with the axial axis, z, anti-parallel to the gravitational acceleration, $\boldsymbol{g}$, is used for both down- and up-flow.

To check the accuracy of the mean axial velocity profiles, the products of the mean axial fluid velocity and the area of each discrete bin, $\langle U_z \rangle_k A_k$, were summed to obtain the mean volumetric flow rate, Q, through the measurement volume. Temperature measurements yielded the water mass density, ρ. The resulting product ρQ corresponded to the mass flow rate given by the Coriolis meter within its accuracy range.

2.3. *Properties of particles*

The properties of the polystyrene particles applied in the present particle-laden experiments are given in table 1. The fluid time scale τ_η at the Stokes number St and the fluid length scale η are the Kolmogorov scales for fully developed single-phase pipe flow at $Re_b = 10\,300$, as computed from DNS results by Veenman (2004). The Kolmogorov length varies between 0.6 mm in the pipe core and 0.2 mm at the wall, whereas the Kolmogorov time varies between 187 ms in the core and 57 ms at the wall. The Reynolds number based on the wall shear velocity and the pipe diameter, Re_τ, is 647. For evaluation of the particle time scale, τ_p, the relaxation time for particles in stationary flow is used; see Albrecht *et al.* (2003):

$$\tau_p = (d_p^2 \rho_p / 18\mu)(1 + 0.5 \rho_f / \rho_p), \tag{2.3}$$

where μ is the dynamic viscosity of the fluid, d_p is the particle diameter and ρ_p and ρ_f are the mass densities of the particles and the fluid respectively. A relaxation time of $\tau_p \approx 4$ ms is obtained for the tracers. It should be noted that the fluid inertia is accounted for by the added mass coefficient 0.5, which close to a wall is increased to approximately 0.7; see van der Geld (2002).

The terminal velocity specified in table 1 is attained in quiescent fluid when the gravitational and drag forces are in equilibrium,

$$U_{TV} = \{4(\rho_p - \rho_f) d_p g / 3 C_D \rho_f\}^{0.5}, \tag{2.4}$$

where g is the gravitational acceleration and C_D is the drag coefficient; it should be noted that U_{TV} is positive by definition. The drag coefficient is a function of the particle Reynolds number, $Re_p = d_p U_{TV} / \nu$, which is based on the particle diameter and the terminal velocity. In the Stokes regime, C_D is given by (2.5). For $1 < Re_p < 1000$, Schiller & Naumann (1935) proposed the correlation given by (2.6),

Particles	Mass density (kg m^{-3})	Diameter d_p (mm)	Terminal velocity, U_{TV}[a] (mm s^{-1})	Re_p	$St = \tau_p/\tau_\eta$ [b]	$St = \tau_p^{+}$[b]	Length-scale ratio: d_p/η[c]
Flow tracers	1050	0.2	1.0	0.18	0.02–0.07	0.10	0.33–1
Inertial particles	1050	0.8	10.2	7.76	0.35–1.11	1.56	1.33–3.5

TABLE 1. The properties of the particles applied in the present particle-laden experiment.

[a]Settling velocity of a particle in an infinite stagnant pool of water.
[b]Kolmogorov time scales for a fully developed single-phase pipe flow at $Re_b = 10\,300$ as computed from the DNS code developed by Veenman (2004): $\tau_\eta \approx 187$ ms at pipe centreline and $\tau_\eta \approx 57$ ms close to the wall. The Stokes number based on the wall shear stress is given by $\tau_p/(\tau_w/\mu) = \tau_p^{+}$, with τ_w the wall shear stress.
[c]Kolmogorov length scales for a fully developed single-phase pipe flow at $Re_b = 10\,300$ as computed from the DNS code developed by Veenman (2004): $\eta \approx 0.60$ mm at pipe centreline and $\eta \approx 0.23$ mm close to the wall.

$$C_D = 24/Re_p, \quad Re_p < 1, \tag{2.5}$$
$$C_D = (24/Re_p)(1 + 1/6 Re_p^{2/3}), \quad 1 < Re_p < 1000. \tag{2.6}$$

The properties of the inertial particles are such that the characteristic root-mean-square velocity representative of the turbulent carrier phase, u_{rms}, and the terminal velocity of the dispersed phase, U_{TV}, are approximately the same, $u_{rms}/U_{TV} = O(1)$.

Since the bulk flow velocity, U_b, is approximately 100 mm s^{-1}, the ratio U_b/U_{TV} is of the order of 10^2 for seeding particles; see table 1. Since $U_b \gg U_{TV}$, $\tau_p < \tau_\eta$ and $d_p < \eta$, the seeding particles employed work well as flow tracers. For the inertial particles, the ratio U_b/U_{TV} is of the order of 10, $\tau_p \approx \tau_f$ and $d_p > \eta$. Therefore, the inertial particles have significant inertial characteristics, as is also exhibited by the differences in the Lagrangian statistical properties, the auto- and cross-correlations of velocities and the accelerations of tracers and inertial particles; see Oliveira *et al.* (2015). These authors showed that the decay of the Lagrangian velocity correlations of the applied inertial particles takes place in shorter times than the decay of the velocity correlation of the flow tracers. The fluctuating velocity of a particle is coherent with the fluid as long as it remains in a characteristic large eddy structure. However, the inertial particles applied here cannot completely follow the large fluid scales due to their inertia (mainly from their finite size) and the acceleration of the fluid volume, which is named added mass. One of the reasons for the difference in tracer and particle behaviour is the so-called crossing trajectory effect, where a particle heavier than the surrounding fluid falls in an external force field, such as gravity, from one eddy to another at a rate faster than the average eddy decay rate. In addition, particles of intermediate size in shear flows experience a hydrodynamic lift.

2.4. Experimental conditions

Downward and upward vertical flows were measured at the same bulk Reynolds number based on the tube diameter, Re_b. The bulk velocity of each flow, U_b, was adapted to temperature changes to keep $Re_b \approx 10\,300$. Single-phase flows served as a reference for two-phase flows. Only tracers were employed in single-phase flow measurements. Both tracers and inertial particles were present in particle-laden measurements. A mean volume fraction of tracers of less than 10^{-6} was applied to

Case	Flow direction	$\langle \Phi_v \rangle$
1S	Upward	0
1A	Upward	0.5×10^{-5}
1B	Upward	1.4×10^{-5}
1C	Upward	3.2×10^{-5}
2S	Downward	0
2A	Downward	1.8×10^{-5}
2B	Downward	2.8×10^{-5}

TABLE 2. The single-phase and particle-laden flow experiments.

Re_b	10 300	—
$Re_\tau{}^a$	647	—
$u_\tau{}^a$	6.47	(mm s^{-1})
ν/u_τ	0.15	(mm)
U_c/U_b	1.28	—
η^a	0.23–0.60	(mm)
$\tau_\eta{}^a$	187–57	(s)
$u_{z,max}{}^b$	16.6	(mm s^{-1})

TABLE 3. Details of the current single-phase pipe flow in fully developed conditions for $U_b = 100$ mm s^{-1} (1S).

[a]As computed from the DNS code developed by Veenman (2004) for the pipe diameter actually used in the experiments.
[b]Maximum root-mean-square fluid velocity. This occurs at $r/R \sim 0.95$ and for the streamwise direction.

all experiments to prevent the enhancement of dissipation effects; see Elghobashi (1994). Particle-laden flows with a mean volume fraction of inertial particles, $\langle \Phi_v \rangle$, ranging from 5.0×10^{-6} to 3.2×10^{-5} were tested.

A particle-laden experimental case is represented here by a number indicating the flow direction (1 or 2) and a letter indicating the mean concentration of inertial particles (A, B or C); see table 2. The reference single-phase flows are 1S and 2S. Details on the single-phase pipe flow based on the scales of the current experiment and in fully developed conditions (case 1S) are presented in table 3. The variables Re_b, Re_τ, U_b, η and τ_η have already been defined above; U_c is the centreline velocity and ν is the fluid kinematic viscosity. The wall shear velocity, u_τ, was derived from DNS data provided by Veenman (2004) by implementing the actual pipe diameter. In the remainder of this work, the bulk velocity U_b is chosen as a normalization quantity instead of the wall shear velocity, u_τ, which is often used in the literature, because U_b can be determined more accurately in our experimental set-up; see § 2.2. The single-phase flow experimental results of Oliveira *et al.* (2013) at $Re_b = 10\,300$ were in accordance with the DNS results. The significance of the pipe flow in relation to the particle motion can be inferred by comparing tables 1 and 3, and by the graphical results in § 3. The maximum root-mean-square fluid velocity occurs at $r/R \sim 0.95$ and for the streamwise direction.

2.5. *Point-particle DNS*

This paper is focused on experimental findings and the interpretation thereof. However, in order to be able to interpret some of the results, we also performed numerical simulations of particle-laden turbulent pipe flow at the same Reynolds number for up-flow. These simulations are not intended to cover the complete physics of the problem, but to complete the understanding of the experimental findings.

In a real DNS, all scales of the flow around each particle should be resolved, which is computationally unfeasible with many particles. Usually, PP-DNS is performed in cases where the number of particles or the range of scales is too large, although PP-DNS is often assumed to be only valid in cases where the particles are small compared with the Kolmogorov scale (Bagchi & Balachandar 2003; Balachandar & Eaton 2010; Vreman 2016), which is certainly not true in our experiments. However, since the particle volume fraction in our experiments is so small that the effects of the particles on the continuous phase are negligible, one-way coupled PP-DNS and a force balance on each particle that includes all relevant forces exerted by the fluid on the particles will be used here. One of the advantages of the one-way coupling is that the liquid velocity and liquid vorticity at the centre of the particle, needed for some of the forces on the particle, are well-defined.

The present section briefly describes the numerical method of the PP-DNS. An Eulerian–Lagrangian approach is applied, where the continuous phase is described in an Eulerian way by the incompressible Navier–Stokes equations in cylindrical coordinates and each particle is tracked in a Lagrangian way by solving its equation of motion. The numerical method for the continuous phase is the same as in Walpot, van der Geld & Kuerten (2007). A pipe with a length equal to $5D$ is used together with periodic conditions in the axial direction. Naturally, the boundary conditions in the tangential direction are periodic as well. A Fourier–Galerkin method is applied in the two periodic directions, and in the radial direction a Chebyshev collocation method is applied, but the radial direction is divided into several elements with a Chebyshev distribution of grid points in each of them to avoid excessive clustering of grid points near the axis of the pipe. The nonlinear terms in the Navier–Stokes equation are calculated in Fourier space making use of the 3/2 rule to avoid aliasing. For the present bulk Reynolds number of 10 300, the numbers of grid points are 150 in the radial direction, 256 in the tangential direction and 384 in the axial direction. It has been shown by Oliveira *et al.* (2013) that this resolution is sufficient to obtain good agreement with experimental results for single-phase flow. Time integration is performed with a second-order-accurate time-splitting method, in which the nonlinear terms are treated explicitly and the viscous and pressure terms implicitly.

At the low particle–fluid mass density ratio considered here, all forces exerted by the fluid on a particle need to be taken into account, but for computational reasons we omit the Basset history force. Therefore, the equation of motion on each particle comprises the buoyancy force, the pressure gradient force, the added mass force, the drag force and the shear lift force,

$$\rho_p V_p \frac{\mathrm{d}\boldsymbol{v}_p}{\mathrm{d}t} = V_p(\rho_p - \rho_f)\boldsymbol{g} + \rho_f V_p \frac{\mathrm{D}\boldsymbol{U}}{\mathrm{D}t} + \rho_f V_p C_{AM} \left[\frac{\mathrm{D}\boldsymbol{U}}{\mathrm{D}t} - \frac{\mathrm{d}\boldsymbol{v}_p}{\mathrm{d}t} \right]$$
$$- (1/8)\rho_f C_D \pi d_p^2 |\boldsymbol{v}_p - \boldsymbol{U}|(\boldsymbol{v}_p - \boldsymbol{U}) - \rho_f V_p C_L (\boldsymbol{v}_p - \boldsymbol{U}) \times \boldsymbol{\omega}. \quad (2.7)$$

The vorticity of the flow field, $\nabla \times \boldsymbol{U}$, is denoted by $\boldsymbol{\omega}$, and $\mathrm{D}\boldsymbol{U}/\mathrm{D}t$ represents the Lagrangian fluid acceleration, which is the sum of the pressure gradient acceleration

and a viscous deceleration,

$$\frac{\mathrm{D}\boldsymbol{U}}{\mathrm{D}t} = \frac{\partial \boldsymbol{U}}{\partial t} + \boldsymbol{U} \cdot \nabla \boldsymbol{U}. \tag{2.8}$$

The undisturbed fluid velocity, $\boldsymbol{U}(\boldsymbol{x}_p)$, is by definition at the location of the centre of mass of the particle, $\boldsymbol{x}_p$. The coefficients C_{AM}, C_D and C_L denote the added mass, drag and lift coefficients respectively. The coefficient C_{AM} is taken to be 0.5, C_D is computed with the Schiller & Naumann (1935) correlation given by (2.5) and (2.6), and C_L is given by the following correlation, valid for low Reynolds numbers $Re_s = d_p^2 |\boldsymbol{\omega}| \rho_f / \mu$ (van der Geld 1997):

$$C_L = 3.084/\sqrt{Re_s}. \tag{2.9}$$

In order to obtain the fluid velocity, vorticity and acceleration at the particle position, tri-linear interpolation is applied. Stability problems near the pipe axis are prevented by using the equations for the Cartesian components of particle position and velocity. Moreover, for the particles, periodic conditions are applied in the axial direction. Particles collide elastically with the wall of the pipe. The number of particles tracked in the simulation is larger than in the experiments. Since only one-way coupling is applied, this does not change the results but does increase the statistical accuracy of the results.

The simulation is started from a fully developed turbulent flow to which particles are added at random positions, uniformly distributed over the whole volume of the pipe. The initial velocity of a particle is equal to the velocity of the fluid at the position of the particle. Statistical results for the particle properties are gathered after a statistically steady particle volume fraction distribution in the radial direction has been reached. Simulations are only performed for up-flow. For down-flow, the lift force leads to a strong motion of particles towards the wall of the pipe, resulting in a locally high particle concentration, so that two-way coupling and particle collisions cannot be disregarded.

3. Results and discussion

In this section, the experimental results will be presented and an interpretation will be given which is also based on a comparison with PP-DNS results and experimental results for single-phase flow. The focal points are the particle volume fraction profile, the mean axial relative velocity profile and the Reynolds stress tensors of the fluid and the particles. First, it will be investigated to what extent the velocity statistics obtained in the measurement section correspond to fully developed conditions.

3.1. *Assessment of the extent of flow development*

Especially for the experiments in down-flow, the distance between the flow straightener and the measurement section might be too small to obtain fully developed flow in the measurement section. Therefore, we will first investigate to what extent the velocity statistics obtained for single-phase flow correspond to fully developed results obtained by means of DNS (Veenman 2004; Walpot *et al.* 2007) at the same Reynolds number. The diagonal components of the Reynolds stress tensor of the single-phase results for up-flow will be seen to correspond well with the DNS results, which indicates that this flow is indeed fully developed; see also Oliveira *et al.* (2013). However, deviations of up to 15 % will be seen to occur in the results
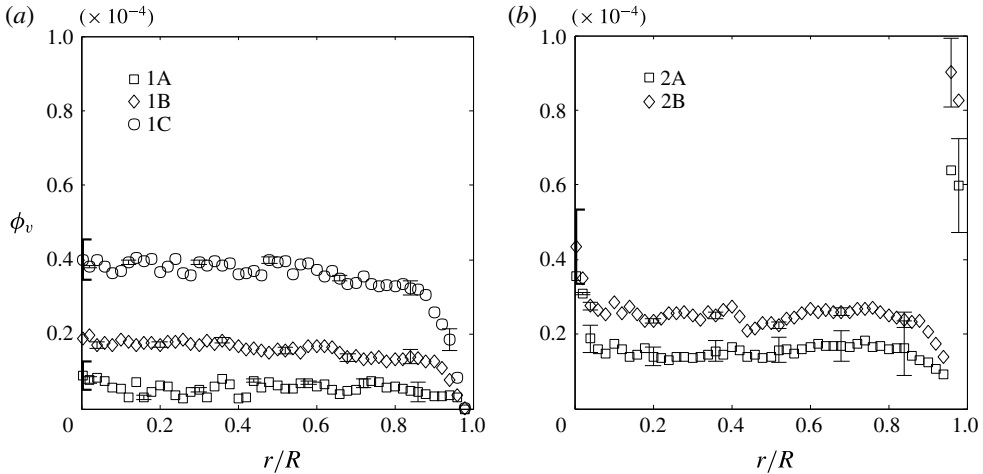
FIGURE 3. Volume fraction profiles of inertial particles, $\phi_v(r/R)$, for various values of the mean particle volume fraction. (*a*) Up-flow; (*b*) down-flow.

for down-flow, which can only be explained by a too small distance between the flow straightener and the measurement section, which equals 20*D*. The deviations are restricted to the regions close to their maxima, i.e. $0.6 < r/R < 0.9$. Moreover, the mean axial velocity profiles differ by only 2 % at most. Although a well-known correlation predicts that the entrance length equals approximately 20*D* in the present experiment (Hinze 1975), this distance is apparently insufficient for a fully developed flow in all respects. Nevertheless, the magnitude and extent of the deviations of the experimental single-phase down-flow results from fully developed flow (DNS or up-flow) are sufficiently small to discriminate important trends in the behaviour of inertial particles, as will be shown in this paper. In addition, the results of the present research can be applied to validate DNS results on particle-laden flow.

It should be noted that the development length of two-phase flow is generally larger than that of single-phase flow. Therefore, the observation that the single-phase up-flow is fully developed does not imply that the particle concentration in the corresponding two-phase flow is fully developed in the measurement section. This will be investigated in the next section.

3.2. *Volume fraction profiles of inertial particles*

In this section, we will first investigate the particle volume fraction profiles for both up-flow and down-flow and then give an explanation for the observed behaviour by considering the particle equation of motion. Figure 3 shows the particle volume fraction as a function of the radial coordinate for up-flow and down-flow and for all mean particle volume fractions studied. The error bars have a size of ± 2 times the standard error. A sample corresponds to the instantaneous volume fraction found in one measurement for a given radial position, and the mean volume fraction corresponds to the time-averaged volume fraction of particles at this same location.

The results presented in figure 3 are consistent: the volume fraction profiles are hardly affected even when half of the total number of samples is used. Figure 3(*a*) shows that in up-flow, the particle volume fraction is smaller close to the pipe wall,

i.e. for $r/R > 0.85$, than in the centre. For down-flow, on the other hand, a distinct large peak at $r/R \approx 0.97$ is observed. This shows that the volume fraction profile strongly depends on the direction of the flow, in particular in the near-wall zone. The results for down-flow also show a second peak at $r/R = 0$ but with a significantly smaller magnitude than the peak near the wall. This central peak finds its origin in the development of the flow. Just after the flow straightener on top, the velocity profile is close to being uniform. Subsequent development of the flow requires motion towards the centre. This flow carries particles along. Further downstream, this peak will disappear. It should be noted that turbophoresis, particle motion towards the wall of a pipe by the effect of turbulence, cannot explain the concentration results. If this effect was dominant, the concentration profiles in up- and down-flows should be similar.

The observed differences in particle volume fraction profiles between up-flow and down-flow can be explained by the forces exerted on the particles. If the three main forces of the particle equation of motion are retained, equation (2.7) reduces to

$$0 = V_p(\rho_p - \rho_f)\boldsymbol{g} + (1/8)\rho_f C_D \pi d_p^2 |\boldsymbol{v}_p - \boldsymbol{U}|(\boldsymbol{v}_p - \boldsymbol{U}) - \rho_f V_p C_L(\boldsymbol{v}_p - \boldsymbol{U}) \times \boldsymbol{\omega}. \quad (3.1)$$

The main contribution from the vorticity to this equation is through the contribution to its tangential component from the mean axial velocity $\mathrm{d}\langle U_z \rangle / \mathrm{d}r$ close to the wall. The axial component of (3.1) therefore results in $v_{p,z} = U_z - U_{TV}$. The radial component provides a balance between lift and drag and can be simplified to $v_{p,r} = 4 d_p (C_L/C_D) \mathrm{d}\langle U_z \rangle / \mathrm{d}r / 3$. For up-flow, this radial particle velocity is directed towards the centre of the pipe, whereas for down-flow, it is directed towards the wall. Point-particle DNS simulations without lift force resulted in uniform particle concentrations, which confirms the above explanation. Next, we will use force balance (3.1) to estimate the magnitude of the mean radial particle velocity.

If only the dominant forces are retained, the radial component of (3.1) can be written as

$$-(1/8)\rho_f C_D \pi d_p^2 |\boldsymbol{v}_p - \langle \boldsymbol{U} \rangle_L| \langle v_{rel,r} \rangle_L - \rho_f V_p C_L \langle v_{rel,z} \rangle_L \omega_\theta = 0. \quad (3.2)$$

Let $\mathrm{sgn}(\langle U_z \rangle)$ denote the sign of the mean axial velocity component. As will be shown below, the mean value of $|\boldsymbol{v}_p - \langle \boldsymbol{U} \rangle_L|$ is close to U_{TV}. We use the notation $\langle \ \rangle_L$ to indicate a Lagrangian average, i.e. the average value taken over all particles located at a certain radial coordinate. Now, suppose that an inertial particle is moving towards the centre of the tube. The drift velocity of the inertial particles in the radial direction can be defined as the value of $\langle v_{rel,r} \rangle_L$ that follows from (3.2),

$$U_{drift} = \mathrm{sgn}(\langle U_z \rangle) 4 d_p (C_L/C_D) \mathrm{d}\langle U_z \rangle / \mathrm{d}r / 3. \quad (3.3)$$

If the lift force coefficient is taken to be 0.5 and the mean value of $\mathrm{d}\langle U_z \rangle / \mathrm{d}r$ for $0 < r/R < 0.6$ is employed, a drift velocity of 0.1 mm s^{-1} is found, directed towards the wall for down-flow and towards the centre of the pipe for up-flow. The measured mean radial particle velocity is indeed of the order of U_{drift} for $0 < r/R < 0.6$, while for $0.8 < r/R < 1.0$, it is systematically negative in up-flow and positive in down-flow, with absolute maxima of approximately 0.6 mm s^{-1} in both cases.

Upstream of the measurement section, just behind the flow straightener, the inertial particles are still homogeneously distributed over the cross-section of the pipe and no preferential concentration is present yet. At this position, the mean radial fluid velocity evaluated at the particle positions is still equal to the Eulerian mean radial fluid velocity, which is equal to zero. As a result of (3.3), the mean radial particle velocity is directed towards the axis of the pipe for up-flow and towards the pipe wall for down-flow. The measured non-zero radial particle velocity shows that the particle concentration is not yet fully developed in the measurement section.
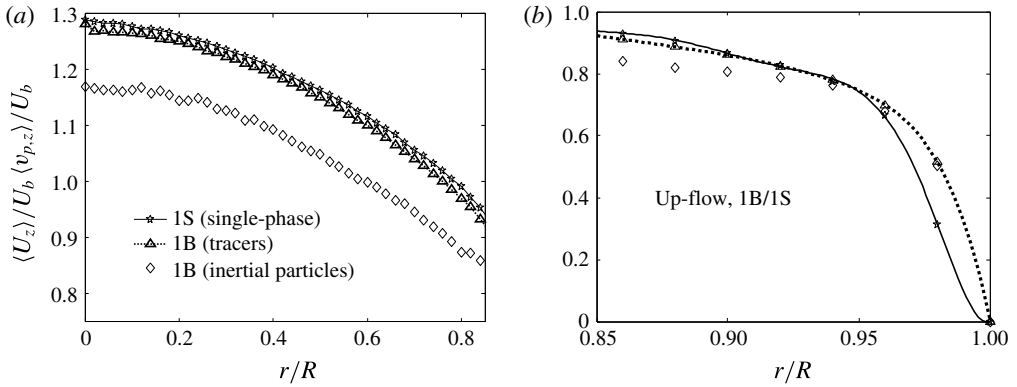
FIGURE 4. Mean axial velocity profiles, $\langle U_z \rangle$ and $\langle v_{p,z} \rangle$, of the particle-laden case 1B and the single-phase flow 1S (up-flow), (*a*) in the range $0 < r/R < 0.85$ and (*b*) in the range $0.85 < r/R < 1$. The velocities are normalized by the bulk velocity of each flow, U_b. The lines are added to guide the eye. The difference in scales should be noted.
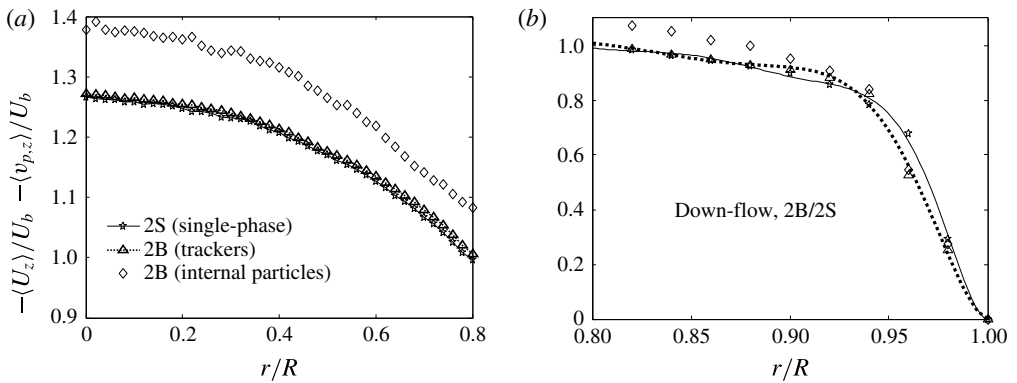

FIGURE 5. Mean axial velocity profiles, $\langle U_z \rangle$ and $\langle v_{p,z} \rangle$, of the particle-laden case 2B and the single-phase flow 2S (down-flow), (*a*) in the range $0 < r/R < 0.8$ and (*b*) in the range $0.8 < r/R < 1$. The velocities are normalized by the bulk velocity of each flow, U_b. The lines are added to guide the eye. The difference in scales should be noted.

3.3. *Mean axial velocity profiles*

Figures 4 and 5 show the mean axial velocity profiles of the fluid, $\langle U_z \rangle$, and the inertial particles, $\langle v_{p,z} \rangle$, for up- and down-flow. All velocities in this paper are normalized with the bulk fluid velocity, U_b, which varies from case to case. The bulk flow velocity was adjusted to keep the bulk Reynolds number for each experiment equal to 10 300. The error bars have sizes comparable to the dimensions of the symbols and are not shown.

The mean axial fluid velocity in two-phase up-flow is slightly smaller than the corresponding single-phase velocity in most of the cross-section of the pipe. This is caused by the particles, which have a smaller velocity, dragging the fluid along. The opposite is observed in figure 5 for down-flow. It should be noted that the cross-sectional average fluid velocity is the same in all cases. Therefore, this small difference in axial velocities is compensated close to the wall (figures 4*b* and 5*b*).
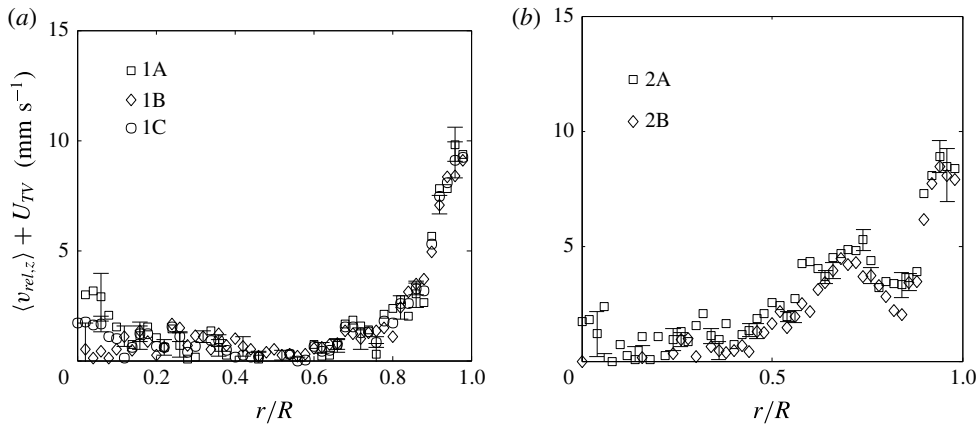
FIGURE 6. The difference between the mean axial particle and fluid velocities, $\langle v_{rel,z} \rangle$, for up-flow (*a*) and down-flow (*b*).

The relative velocity is approximately constant in the range $0 < r/R < 0.5$. This difference is approximately equal to 10.2 mm s^{-1}, which is the value of U_{TV}; see table 1. The difference decreases further away from the pipe axis. For $r/R > 0.90$, the mean fluid and particle velocities are almost equal; see figure 6, where the difference between the relative velocity and the terminal velocity, U_{TV}, is shown as a function of the radial coordinate. Understanding of this finding is facilitated by a study of the PP-DNS results for the same flow. Figure 7 shows various mean axial velocity profiles obtained in the PP-DNS for up-flow. The mean fluid velocity, $\langle U_z \rangle$, the mean particle velocity, $\langle v_{p,z} \rangle$, the mean fluid velocity at the particle positions, $\langle U_z \rangle_L$, and the absolute value of the mean relative velocity, which is defined as $\langle v_{rel,z} \rangle_L = \langle v_{p,z} \rangle - \langle U_z \rangle_L$, are included (mean is here defined as the average over time and the two homogeneous directions). It should be noted that this relative velocity is not accessible in measurements, since it requires the fluid velocity at the particle position, which is not defined. In particle-resolved DNS, this quantity is not defined either, but for this reason we applied PP-DNS.

Figure 7 shows that if $r/R < 0.7$, the difference between $\langle U_z \rangle$ and $\langle U_z \rangle_L$ is negligible, which implies that the mean relative velocity as seen by the particle is equal to U_{TV}. Closer to the wall, the Lagrangian averaged axial fluid velocity starts to deviate from its Eulerian averaged value. Apparently, particles are preferentially located in regions where the axial fluid velocity component has a higher absolute value than the mean fluid velocity. This can be understood in the following way. Consider an inertial particle in developed upward pipe flow outside the core of the pipe. It is driven there by a positive radial fluid velocity fluctuation. Since the Reynolds stress of the fluid is positive, the axial fluid velocity fluctuation must also be positive on average. The instantaneous axial velocity of the particle, v_{pz}, is the sum of the constant $-U_{TV}$ and the fluid velocity, as shown by the PP-DNS results of figure 7. The value of v_{pz} is therefore preferentially shifted to positive values of fluid velocity fluctuations. The lower Eulerian mean relative velocity near the wall also results from this.

A similar finding to that in figure 6(*b*) for the range $r/R < 0.6$, where $-U_{TV} \approx \langle v_{rel,z} \rangle$, was observed by Suzuki *et al.* (2000) in downward channel flow of water with ceramic beads with mass density exceeding the carrier phase by a factor of 3.85. The ratios of the root-mean-square (RMS) fluid velocity to the terminal velocity
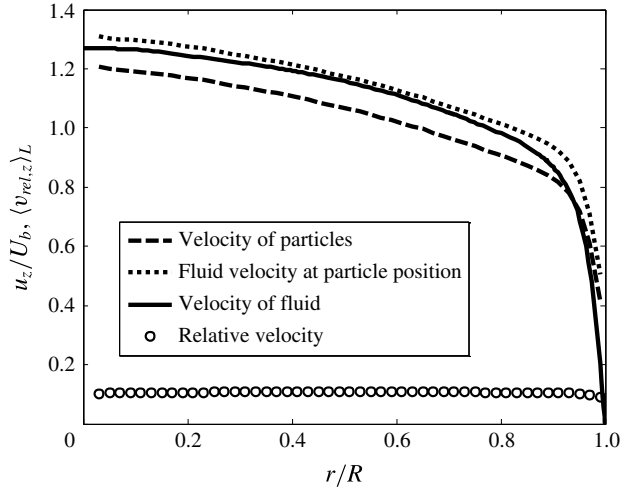
FIGURE 7. Point-particle DNS computations of local mean axial velocity components. The dashed line gives the component of the inertial particles and the dotted line the mean liquid velocity at the particle position. The mean fluid velocity (solid) and the absolute value of the local mean relative velocity as sampled by the particles, $|\langle v_{rel,z}\rangle_L|$ (symbols), are also given.

of the inertial particles, u_{rms}/U_{TV}, in their experiments are close to 0.2, which is different from the value of approximately 1 in the present study. A maximum concentration of inertial particles occurred near the channel walls, similarly to the down-flow measurements presented here, and $|\langle v_{rel,z}\rangle|$ was also found to decrease with decreasing distance from the wall. Suzuki *et al.* (2000) observed that the velocity difference between the carrier phase and the inertial particles is approximately equal to the terminal velocity. Near the wall, they observed a reduction of the relative velocity of approximately 10 % of U_{TV}.

In the next section, it will be shown that the above explanation of the relative velocity is consistent with the interpretation of the particle Reynolds stress tensor.

3.4. *Reynolds stress tensors of the fluid and the dispersed phase*

In this section, the components of the Reynolds stress tensor, R_{ij}, which are averages of the products of velocity fluctuations, with i and j denoting cylindrical coordinates (r, θ, z), are assessed for both phases. We use $R_{ij}^f = \langle u_i u_j \rangle$ for the fluid phase and $R_{ij}^p = \langle v_{pi}' v_{pj}' \rangle$ for the dispersed phase. In fully developed pipe flow, the only decoupled direction is the tangential one, which implies that all cross-correlations involving the tangential velocity are zero, which is confirmed by the experimental results.

The non-zero components of the Reynolds stress tensor are presented in figures 8–10. All results are normalized by the square of the bulk flow velocity of the corresponding experiment. In each plot, the single-phase results are also shown.

In Oliveira *et al.* (2013), the non-zero components of the Reynolds stress tensor of the fluid of case 1S were shown to agree with the DNS results of Veenman (2004). While at the centre of the tube ($r/R < 0.2$) turbulence is nearly homogeneous, highly inhomogeneous behaviour is seen closer to the wall ($0.8 < r/R < 1$); see figures 8 and 9.
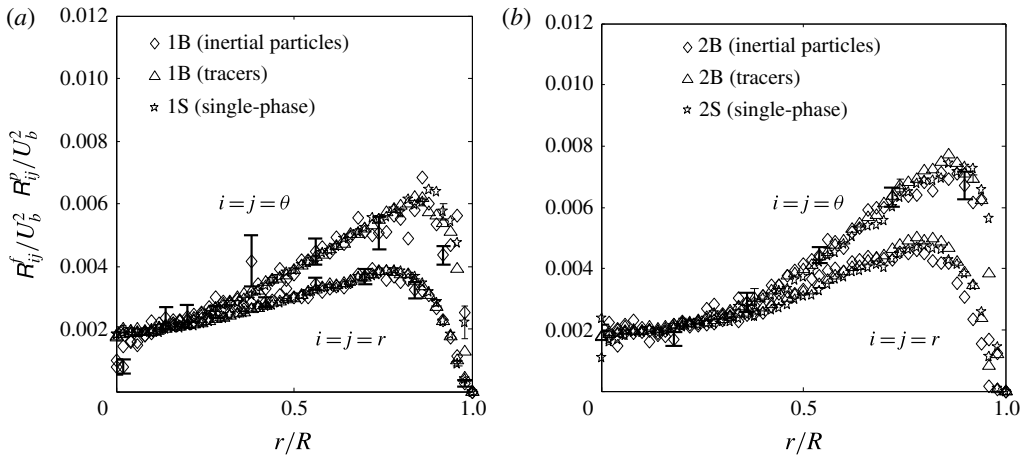
FIGURE 8. Radial and tangential components of the Reynolds stress tensor, R_{rr}^f, R_{rr}^p, $R_{\theta\theta}^f$ and $R_{\theta\theta}^p$, for upward cases 1B/1S (*a*) and downward cases 2B/2S (*b*). The results are normalized by the square of the bulk velocity of each flow, U_b^2. The lines are added to guide the eye.
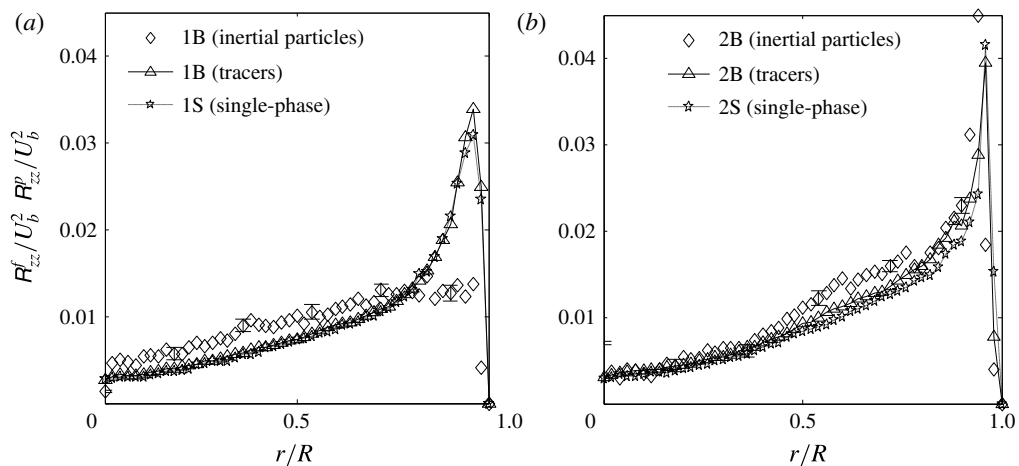

FIGURE 9. Axial components of the Reynolds stress tensor, R_{zz}^f and R_{zz}^p, for upward cases 1B/1S (*a*) and downward cases 2B/2S (*b*). The results are normalized by the square of the bulk velocity of each flow, U_b^2. The lines are added to guide the eye.

Figures 8–10 show that the results for the tracers in particle-laden flow are almost indistinguishable from the single-phase flow results. This shows that the particle concentration in the experiments is so low that the particles do not significantly affect the carrier phase. Therefore, the modification of flow turbulence is not of concern in the present study due to the low concentration of particles applied. The noisy character of the symbols for the Reynolds stresses of the inertial particles in figures 8–10 can be attributed to the number of velocity samples: 2×10^6 velocity vectors for tracers and only 3×10^5 for inertial particles in each particle-laden case; see §2.2.
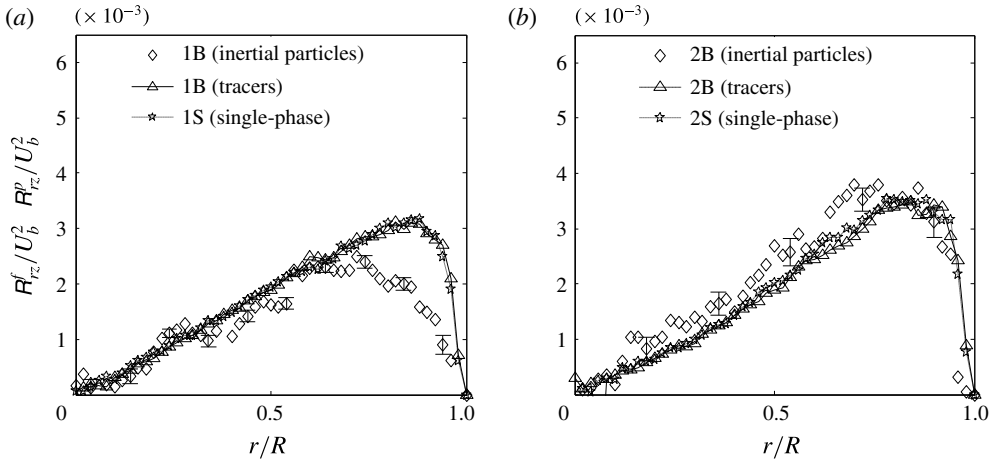
FIGURE 10. Non-diagonal components of the Reynolds stress tensor, R_{rz}^f and R_{rz}^p, for upward cases 1B/1S (*a*) and downward cases 2B/2S (*b*). The results are normalized by the square of the bulk velocity of each flow, U_b^2. The lines are added to guide the eye.

The radial and tangential diagonal components of the Reynolds stress tensor of the dispersed phase are almost equal to the corresponding results for the carrier phase for both up-flow (figure 8*a*) and down-flow (figure 8*b*). However, the diagonal axial and non-zero non-diagonal components of the Reynolds stress tensor of the fluid and the dispersed phase are not equal. In the range $r/R < 0.8$, R_{zz}^p exceeds R_{zz}^f by more than 20 % for up-flow (figure 9*a*) and by more than 15 % down-flow (figure 9*b*). For $r/R > 0.8$ in up-flow, both R_{rz} and R_{zz} for the particles are significantly smaller than for the fluid.

In order to explain this observed behaviour of the Reynolds stress tensor of the dispersed phase for $r/R > 0.8$, we invoke the concept of turbulent diffusion. Turbulent diffusion theory establishes a relation between the non-diagonal component of the Reynolds stress tensor and the radial derivative of the axial fluid velocity of the form

$$\langle u_r u_z \rangle = -\Gamma_T \partial \langle U_z \rangle / \partial r. \tag{3.4}$$

The closure (3.4) is only approximate but offers a convenient way to qualitatively understand the phenomenon of turbulent diffusion. Since $d\langle U_z \rangle / dr < 0$ in pipe flow, this relation shows that $R_{rz}^f > 0$. Next, we turn to the particle Reynolds stress. Due to the direction of the lift force from the wall to the centre of the pipe, particles near the wall in up-flow are mainly driven by sweeps from the centre to the wall. For $r/R > 0.7$, these particles are therefore in eddies that carry a lower absolute value of the velocity gradient $d\langle U_z \rangle / dr$. This is why the Lagrangian sampled average of this gradient, $|\langle dU_z/dr \rangle_L|$, is smaller than the Eulerian average. The results of the PP-DNS, shown in figure 11(*a*), confirm this.

The probability density function (p.d.f.) of the Lagrangian sampled $\partial U_z / \partial r$ at $r/R = 0.9$, shown in figure 11(*b*), is a further illustration of this. This figure also shows the Eulerian average (approximately $-2U_b/R$, indicated by the vertical line). Diffusion theory for both the fluid and particle Reynolds stresses (3.4) now explains why $R_{rz}^p < R_{rz}^f$ close to the wall.
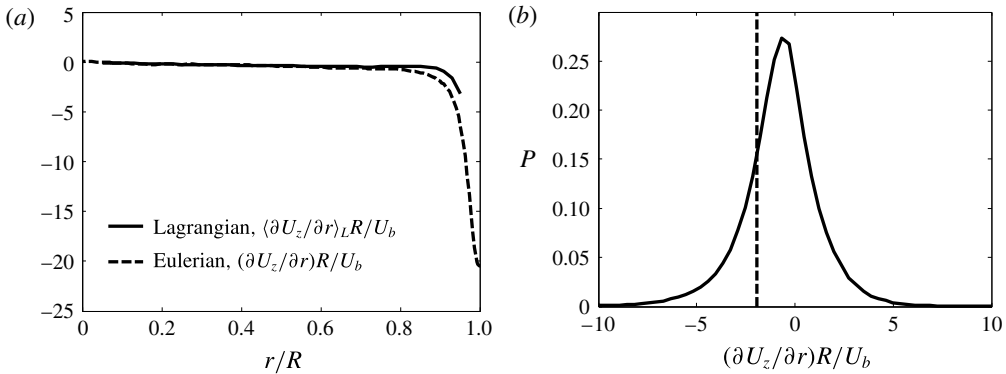
FIGURE 11. Comparison of $\langle \partial U_z / \partial r \rangle_L$ and $\partial \langle U_z \rangle / \partial r$, made dimensionless with the tube radius (R) and bulk velocity (U_b), as computed by PP-DNS (*a*); probability density, P, of $(\partial U_z / \partial r) R / U_b$ (*b*).
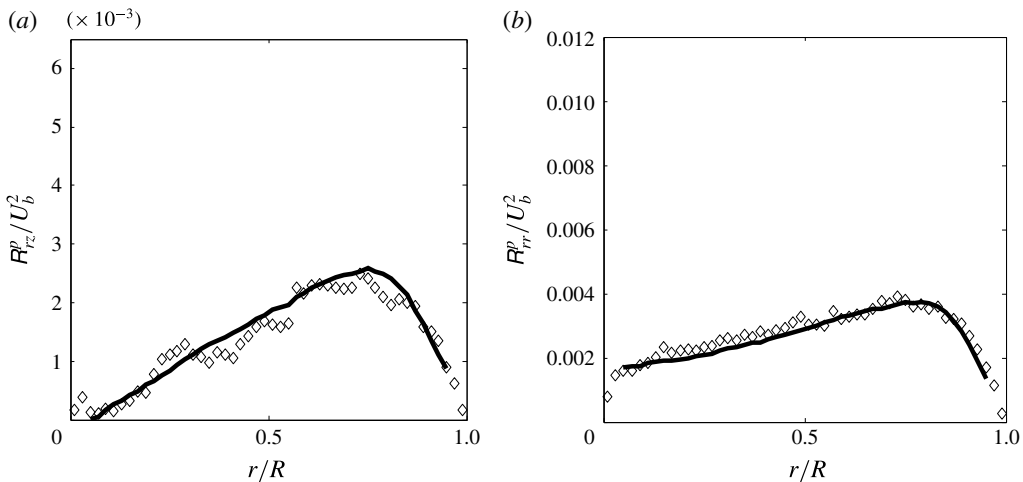

FIGURE 12. Reynolds stress tensor components measured in up-flow (symbols) and computed for the particles with the point-force model in PP-DNS (solid line).

At the same time, the Reynolds stress R_{zz} of inertial particles outside the core of the pipe is less than for fluid particles (figure 9*a*). This is substantiated by the PP-DNS results, which indeed showed that $\langle U_z \rangle_L$ exceeds the Eulerian counterpart $\langle U_z \rangle$ (figure 7), while the Reynolds particle stresses are close to the experimental values; see figure 12.

In contrast to up-flow, in down-flow and close to the wall, particles are not mainly driven by sweeps from the wall to the centre, since other mechanisms force particles away from the wall. Because of the large local particle concentration, diffusion is stronger near the wall than in the core. In addition, an inertial particle must also bounce at the wall. The Lagrangian average of dU_z / dr is therefore about the same as the Eulerian average. As a consequence, the Reynolds stresses R_{rz}^p and R_{zz}^p of inertial particles are close to the corresponding fluid Reynolds stresses.

For $r/R < 0.8$, the particle Reynolds stresses are 15 % larger (figures 9*b* and 10*b*). The reason for this is probably that the down-flow case is not fully developed.

This has been verified by the observation that upon removing the flow straightener at the inlet, as presented in Oliveira (2012), the turbulent stresses become higher.

4. Conclusions

In this paper, turbulent particle-laden pipe flow has been studied by means of 3D-PTV. We considered particles that have a slightly larger mass density than the fluid and a size larger than the Kolmogorov scale. The ratio of the RMS fluid velocity to the terminal velocity of the inertial particles is of order 1; $u_{rms}/U_{TV} = O(1)$. Results have been obtained for both up-flow and down-flow, and for both tracer and inertial particles. For up-flow, the results have been compared with results of PP-DNS, using particle tracking and including all forces.

Two major findings were made:

(i) the inertial particle concentration is high near the wall in down-flow and high near the centre in up-flow;

(ii) the axial component of the mean relative velocity decreases to zero near the wall in both cases.

We showed that the shear lift force is the only possible explanation for the first finding. The second finding is explained by the preferential location of inertial particles in upward moving parts of near-wall eddies. Other findings concern the turbulent stresses of both fluid and inertial particles and are consistent with these two explanations.

Acknowledgements

Appendix. State of development in up-flow and down-flow

In this appendix, we will discuss the state of development of the up-flow and down-flow measured at the test location. In Oliveira *et al.* (2013), it has already been shown, by comparison of the velocity profile and Reynolds stress tensors with those of DNS, that the up-flow is fully developed. In the up-flow case, the distance between the flow straightener and the measurement section is $45D$, whereas this distance is only $20D$ for down-flow. In the down-flow case, the inlet section contains a flow straightener consisting of a set of parallel tubes; each tube has an inner diameter of 5 mm and a length of 40 cm; see figure 13.

The state of development was investigated by comparing the flow characteristics of down-flow with and without a flow straightener with results from DNS and up-flow. As a typical example, R_{zz}^f is shown for all of these cases in figure 14. The figure shows that the up-flow results agree very well with the DNS results, in agreement with the conclusion in Oliveira *et al.* (2013). Down-flow with a flow straightener results in somewhat higher velocity fluctuations, particularly in the peak close to the wall. Removal of the flow straightener leads to a significant further increase of the velocity fluctuations over the whole radius of the pipe. It is obvious that the less developed the flow is, the higher the velocity fluctuations are. The relatively small difference between the up-flow and down-flow cases with a flow straightener indicates that the down-flow is close to being fully developed.
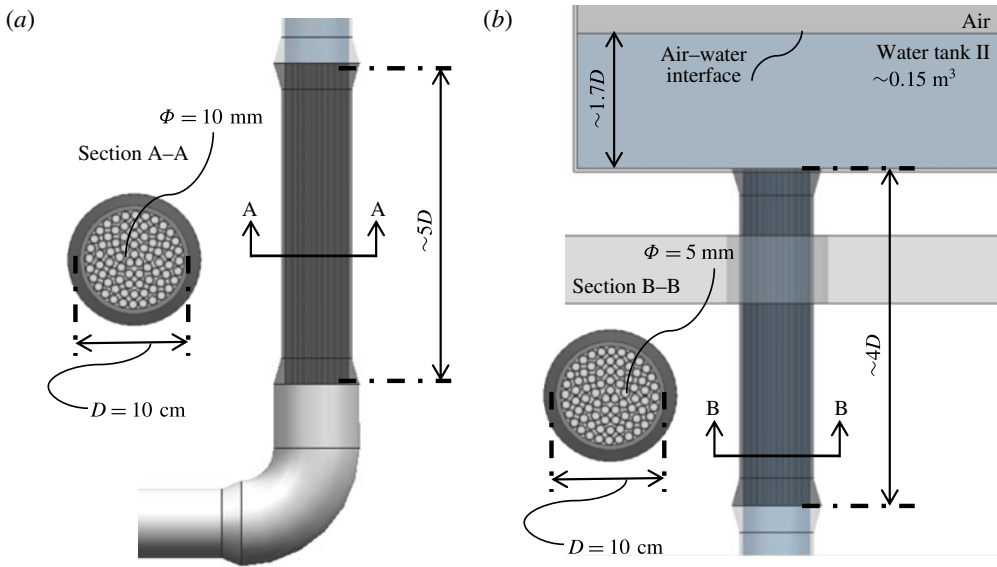
FIGURE 13. (Colour online) Schematics of the flow straighteners and inlet sections for up-flow (*a*) and down-flow (*b*).
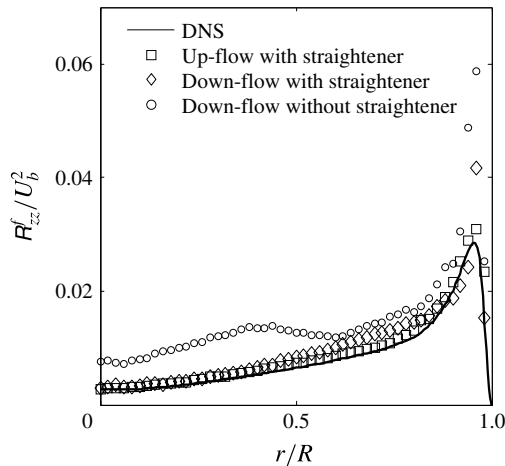

FIGURE 14. Comparison of the axial diagonal component of the Reynolds stress tensor between DNS, up-flow and down-flow.

REFERENCES

ALBRECHT, H.-E., BORYS, M., DAMASCHKE, N. & TROPEA, C. 2003 *Laser Doppler and Phase Doppler Measurement Techniques*. Springer.

ALISEDA, A. & LASHERAS, J. C. 2011 Preferential concentration and rise velocity reduction of bubbles immersed in a homogeneous and isotropic turbulent flow. *Phys. Fluids* **23**, 093301.

AUTON, T. R. 1987 The lift force on a spherical rotational flow. *J. Fluid Mech.* **183**, 199–218.

AUTON, T. R., HUNT, J. C. R. & PRUD'HOMME, M. 1988 The force exerted on a body in inviscid unsteady non-uniform rotational flow. *J. Fluid Mech.* **197**, 241–257.

BAGCHI, P. & BALACHANDAR, S. 2003 Effect of turbulence on the drag and lift of a particle. *Phys. Fluids* **15**, N11.

BALACHANDAR, S. & EATON, J. K. 2010 Turbulent dispersed multiphase flow. *Annu. Rev. Fluid Mech.* **42**, 111–133.

BENSON, M., TANAKA, T. & EATON, J. K. 2005 The effects of wall roughness on particle velocities in a turbulent channel flow. *Trans. ASME J. Fluids Engng* **127**, 250–256.

BORÉE, J. & CARAMAN, N. 2005 Dilute bidispersed tube flow: role of interclass collisions at increased loadings. *Phys. Fluids* **17**, 055108.

BROWN, R. D., WARHAFT, Z. & VOTH, G. A. 2009 Acceleration statistics of neutrally buoyant spherical particles in intense turbulence. *Phys. Rev. Lett.* **103** (19), 194501.

CALZAVARINI, E., VOLK, R., BOURGOIN, M., LÉVÊQUE, E., PINTON, J.-F. & TOSCHI, F. 2009 Acceleration statistics of finite-sized particles in turbulent flow: the role of Faxén forces. *J. Fluid Mech.* **630**, 179–189.

CARAMAN, N., BORÉE, J. & SIMONIN, O. 2003 Effect of collisions on the dispersed phase fluctuation in a dilute tube flow: experimental and theoretical analysis. *Phys. Fluids* **15** (12), 3602–3612.

DIJKHUIZEN, W., VAN SINT ANNALAND, M. & KUIPERS, J. A. M. 2010 Numerical and experimental investigation of the lift force on single bubbles. *Chem. Engng Sci.* **65**, 1274–1287.

DRACOS, T. 1996 Particle tracking in three-dimensional space. In *Three-dimensional Velocity and Vorticity Measuring in Image Analysis Techniques* (ed. Th. Dracos), Kluwer Academic.

ELGHOBASHI, S. 1994 On predicting particle-laden turbulent flows. *Appl. Sci. Res.* **52**, 309–329.

VAN DER GELD, C. W. M. 1997 Measurement and prediction of solid sphere trajectories in accelerated gas flow. *Intl J. Multiphase Flow* **23** (2), 357–376.

VAN DER GELD, C. W. M. 2002 On the motion of a spherical bubble deforming near a plane wall. *J. Engng Maths* **42** (2), 91–118.

HINZE, J. O. 1975 *Turbulence*. McGraw-Hill.

KULICK, J. D., FESSLER, J. R. & EATON, J. K. 1994 Particle response and turbulence modification in fully developed channel flow. *J. Fluid Mech.* **277**, 109–134.

KUNKEL, A. J. J. & SMITS, A. J. M. 2007 Further support for Townsend's Reynolds number similarity hypothesis in high Reynolds number rough-wall pipe flow. *Phys. Fluids* **19**, 055109.

KUSSIN, J. & SOMMERFELD, M. 2002 Experimental studies on particle behaviour and turbulence modification in horizontal channel flow with different wall roughness. *Exp. Fluids* **33**, 143–159.

LEGENDRE, D. & MAGNAUDET, J. 1998 The lift force on a spherical bubble in a viscous linear shear flow. *J. Fluid Mech.* **368**, 81–126.

LUCAS, D. & TOMIYAMA, A. 2011 On the role of the lateral lift force in poly-dispersed bubbly flows. *Intl J. Multiphase Flow* **37**, 1178–1190.

MAAS, H.-G. 1996 Contributions of digital photogrammetry to 3D-PTV. In *Three-dimensional Velocity and Vorticity Measuring in Image Analysis Techniques* (ed. Th. Dracos), Kluwer Academic.

MAZZITELLI, I. M., LOHSE, D. & TOSCHI, F. 2003 On the relevance of the lift force in bubbly turbulence. *J. Fluid Mech.* **488**, 283–313.

MILLER, R. W. 1996 *Flow Measurement Engineering Handbook*, 3rd edn. McGraw-Hill.

MINIER, J.-P. 2015 On Lagrangian stochastic methods for turbulent polydisperse two-phase reactive flows. *Prog. Energy Combust. Sci.* **50**, 1–62.

OLIVEIRA, J. L. G. 2012 3D-PTV of particle-laden turbulent pipe flows, PhD thesis, Technische Universiteit Eindhoven.

OLIVEIRA, J. L. G., VAN DER GELD, C. W. M. & KUERTEN, J. G. M. 2013 Lagrangian and Eulerian statistics of pipe flows measured with 3D-PTV at moderate and high Reynolds numbers. *Flow Turbul. Combust.* **91** (1), 105–137.

OLIVEIRA, J. L. G., VAN DER GELD, C. W. M. & KUERTEN, J. G. M. 2015 Lagrangian velocity and acceleration statistics of fluid and inertial particles measured in pipe flow with 3D particle tracking velocimetry. *Intl J. Multiphase Flow* **73**, 97–107.

PARIS, A. D. & EATON, J. K. 2001 Turbulence attenuation in a particle-laden channel flow. *Tech. Rep.* TSD-137. Stanford University.

PICANO, F., BREUGEM, W.-P. & BRANDT, L. 2015 Turbulent channel flow of dense suspensions of neutrally buoyant spheres. *J. Fluid Mech.* **764**, 463–487.

POELMA, C. 2004 Experiments in particle-laden turbulence – simultaneous particle/fluid measurements in grid-generated turbulence using particle image velocimetry. PhD thesis, Delft University of Technology.

POPE, S. B. 2000 *Turbulent Flows*. Cambridge University Press.

QURESHI, N. M., BOURGOIN, M., BAUDET, C., CARTELLIER, A. & GAGNE, Y. 2007 Turbulent transport of material particles: an experimental study of finite size effects. *Phys. Rev. Lett.* **99** (18), 184502.

SAFFMAN, P. G. 1965 The lift on a small sphere in a slow shear flow. *J. Fluid Mech.* **22**, 385–400.

SATO, Y. & HISHIDA, K. 1996 Transport process of turbulence energy in particle-laden turbulent flow. *Intl J. Heat Fluid Flow* **17**, 202–210.

SCHILLER, L. & NAUMANN, Z. 1935 A drag coefficient correlation. *Z. Verein. Deutsch. Ing.* **77**.

SENE, K. J., HUNT, J. C. R. & THOMAS, N. H. 1994 The role of coherent structures in bubble transport by turbulent shear flows. *J. Fluid Mech.* **259**, 219–240.

SPELT, P. D. M. & BIESHEUVEL, A. 1997 On the motion of gas bubbles in homogeneous isotropic turbulence. *J. Fluid Mech.* **336**, 221–244.

SUZUKI, Y., IKENOYA, M. & KASAGI, N. 2000 Simultaneous measurements of fluid and dispersed phases in a particle-laden turbulent channel flow with the aid of 3-D PTV. *Exp. Fluids* **29**, 185–193.

TRYGGVASON, G., BUNNER, B., ESMAEELI, A., JURIC, D., AL-RAWAHI, N., TAUBER, W., HAN, J., NAS, S. & JAN, Y.-J. 2001 A front-tracking method for the computations of multiphase flow. *J. Comput. Phys.* **169**, 708–759.

TSUJI, Y. & MORIKAWA, Y. 1982 LDV measurements of an air–solid two-phase flow in a horizontal pipe. *J. Fluid Mech.* **120**, 385–409.

TSUJI, Y., MORIKAWA, Y. & SHIOMI, H. H. 1984 LDV measurements of an air–solid two-phase flow in a vertical pipe. *J. Fluid Mech.* **139**, 417–434.

VEENMAN, M. P. B. 2004 Statistical analysis of turbulent pipe flow: a numerical approach. PhD thesis, Technische Universiteit Eindhoven.

VOLK, R., CALZAVARINI, E., LÉVÊQUE, E. & PINTON, J.-F. 2011 Dynamics of inertial particles in a turbulent von Kármán flow. *J. Fluid. Mech.* **668**, 223–235.

VOTH, G. A., LA PORTA, A., CRAWFORD, A. M., ALEXANDER, J. & BODENSCHATZ, E. 2002 Measurement of particle accelerations in fully developed turbulence. *J. Fluid Mech.* **469**, 121–160.

VREMAN, A. W. 2016 Particle-resolved direct numerical simulation of homogeneous isotropic turbulence modified by small fixed spheres. *J. Fluid Mech.* **796**, 40–85.

WALPOT, R. J. E., VAN DER GELD, C. W. M. & KUERTEN, J. G. M. 2007 Determination of the coefficient of Langevin models for inhomogeneous turbulent flows by 3D PTV and DNS. *Phys. Fluids* **19**, 045102.

YANG, T. S. & SHY, S. S. 2005 Two-way interaction between solid particles and homogeneous air turbulence: particle settling rate and turbulence modification measurements. *J. Fluid Mech.* **526**, 171–216.